MNRAS 000, 1–12 (2016) Preprint 11 March 2020 Compiled using MNRAS LATEX style file v3.0

On the early evolution of massive star clusters: the case of cloud D1 and its embedded cluster in NGC 5253

Sergiy Silich ⋆[1], Guillermo Tenorio-Tagle[1], Sergio Martínez-González[2], Jean Turner[3]
[1] Instituto Nacional de Astrofísica Óptica y Electrónica, AP 51, 72000 Puebla, México
[2] CONACYT-Instituto Nacional de Astrofísica, Óptica y Electrónica, AP 51, 72000 Puebla, México
[3] Department of Physics and Astronomy, UCLA, Los Angeles CA 90095-1547 USA

Accepted XXX. Received YYY; in original form ZZZ

ABSTRACT

We discuss a theoretical model for the early evolution of massive star clusters and confront it with the ALMA, radio and infrared observations of the young stellar cluster highly obscured by the molecular cloud D1 in the nearby dwarf spheroidal galaxy NGC 5253. We show that a large turbulent pressure in the central zones of D1 cluster may cause individual wind-blown bubbles to reach pressure confinement before encountering their neighbors. In this case stellar winds are added to the hot shocked wind pockets of gas around individual massive stars that leads them to meet and produce a cluster wind in time-scales less than 10^5 yrs. In order to inhibit the possibility of cloud dispersal, or the early negative star formation feedback, one should account for mass loading that may come, for example, from pre-main sequence (PMS) low-mass stars through photo-evaporation of their proto-stellar disks. Mass loading at a rate in excess of $8{\times}10^{-9}$ $M_\odot$ yr^{-1} per each PMS star is required to extend the hidden star cluster phase in this particular cluster. In this regime, the parental cloud remains relatively unperturbed, while pockets of molecular, photoionized and hot gas coexist within the star forming region. Nevertheless, the most likely scenario for cloud D1 and its embedded cluster is that the hot shocked winds around individual massive stars should merge at an age of a few millions of years when the PMS star proto-stellar disks vanish and mass loading ceases that allows a cluster to form a global wind.

Key words: galaxies: star clusters — Galaxies individual: NGC 5253 — Physical Data and Processes: hydrodynamics

1 INTRODUCTION

Most stars form in clusters. However only a small fraction of these clusters survives for a long time (Gyrs) as globular clusters (GCs) (see Portegies Zwart et al. 2010). It was suggested that most massive young stellar clusters observed in our local group of galaxies may constitute present-day proto-globular clusters (Elmegreen & Efremov 1997). However so far it is not clear if multiple stellar populations with peculiar chemical patterns (e.g. Lee et al. 1999; Bedin et al. 2004; Marino et al. 2008; Carretta et al. 2009; Renzini et al. 2015) are formed in present-day massive clusters as it occurred long ago in globular clusters or in this respect present-day and globular cluster populations are different and thus star formation deeply depends on their environment conditions.

There are two major scenarios of how star formation proceeds in star cluster progenitor clouds (e.g. Longmore et al. 2014; Banerjee & Kroupa 2015). In an in situ, monolithic formation scenario stellar clusters form in extremely dense and compact progenitor clouds. In a hierarchical or conveyor-belt scenario star formation occurs in the densest peaks spread over the natal pre-stellar cloud. The centrally concentrated cluster is then formed due to infalling and merging of such subclusters in the central zone of the star forming region.

During their early evolution star clusters remain deeply embedded into their parental molecular clouds and are not observable in the visible line regime (see a phenomenological classification scheme by Whitmore et al. 2011). However, stellar winds and the ionizing radiation from massive stars are believed to play a major role in star cluster formation (e.g. Krause et al. 2012; Dale et al. 2015; Calura et al. 2015; Rahner et al. 2017). Indeed, neighboring wind collisions and the residual gas ionization by massive stars boost the gas pressure and result in the formation of a global star cluster wind, the residual gas expulsion from the star forming

⋆ E-mail: silich@inaoep.mx

region (the process, which is usually referred as a negative star formation feedback) and the young cluster emerging in the UV and visible line regimes.

The impact of negative stellar feedback on the parental molecular cloud is crucial as the residual gas contributes significantly to the gravitational field of star forming clouds and its rapid expulsion promotes cluster dissolution in a short time-scale (infant mortality, see Boily & Kroupa 2003; Baumgardt & Kroupa 2007; Portegies Zwart et al. 2010) that does not allow the long-lived, proto-globular clusters to form.

Some observations strongly support this scenario. For example, Bastian et al. (2014); Bastian & Lardo (2015) were unable to find any significant amount of residual gas in their sample of young massive clusters and concluded that even high-mass clusters expel the natal gas within a few Myrs after their formation. High resolution survey of the molecular gas distribution around star forming regions in Large Magellanic Cloud led Seale et al. (2012) to conclude that young clusters destroy their natal molecular clouds on a time-scale of at least a few times 10^5yr. This conclusion strongly restricts scenarios for globular and bound clusters formation.

However, recent observations of nearby galaxies in infrared, millimeter and radio wavelengths revealed an obscured mode of star formation in such galaxies as SBS 0335-052 (Thuan et al. 1999), He 2-10 (Vacca et al. 2002), NGC 2366 (Oey et al. 2017) and NGC 5253 (Turner et al. 2015; Beck 2015; Turner et al. 2017; Cohen et al. 2018). The extension of the hidden star cluster phase is also required in some models of the multiple stellar generations formation in globular clusters (e.g. Kim & Lee 2018; Tenorio-Tagle et al. 2019).

Thus, the current understanding of the physical processes involved in different star cluster formation scenarios remains incomplete. The disruption of natal gas clouds by stellar winds and the residual gas expulsion at early stages of the star cluster assembling, the characteristic time-scale for the global star cluster wind development and mechanisms which may suppress or delay the progenitor cloud disruption are still between the intensively debated problems (see Krause et al. 2012; Calura et al. 2015; Tenorio-Tagle et al. 2015; Krause et al. 2016; Silich & Tenorio-Tagle 2017, 2018; Wünsch et al. 2017; Szécsi & Wünsch 2019).

Recent hydrodynamical simulations of gas-rich galaxies merging allowed one to model star cluster formation down to $4\,M_\odot$ and 0.1pc space resolution (Lahén et al. 2019, 2020). However, the disruptive effects of massive star winds on the star forming cloud and the impact of low mass star outflows on the gas dynamics are still beyond the scope of these simulations.

Silich & Tenorio-Tagle (2017, 2018) discussed the interplay among young massive stars and the residual gas in young stellar clusters semi-analytically that allowed them to study stellar winds dynamics at much smaller scales. They concluded that in compact and massive star-forming clouds wind-driven shells around individual massive stars may stall before merging and hot shocked winds may be pressure confined due to a high intra-cloud gas pressure and strong radiative cooling. This suppresses star cluster winds and prevents the residual gas expulsion from the star-forming cloud. However, the model predictions are sensitive to the star cluster size, which is the "hardest parameter to measure in extragalactic sources" (Beck 2015). Therefore, one has to confront model predictions with observations of young stellar clusters in nearby galaxies provided with an extreme spatial resolution.

Probably, the best example of such a cluster is a young stellar cluster in the nearby dwarf spheroidal galaxy NGC 5253 which is deeply embedded into a dense molecular cloud D1 and coincides with an extremely bright in radio and IR wavebands supernebula (Turner et al. 2000; Turner & Beck 2004; Gorjian et al. 2001; Alonso-Herrero et al. 2004; Beck 2015). The NGC 5253 radio continuum is almost entirely thermal (Beck et al. 1996) that indicates the youth of NGC 5253 clusters, unless their most massive stars collapsed directly into black holes without exploding as supernovae (e.g. Adams et al. 2017a,b; Mirabel 2017a,b).

The supernebula is very compact, with $\sim 0".1$ FWHM that corresponds to $\approx$ 1.9 pc at the distance of 3.8 Mpc adopted to NGC 5253 and extremely bright, accounting for about 1/2 of the entire galaxy IR luminosity (Gorjian et al. 2001). It is located in the center of a compact ($\sim 0".3$ FWHM) molecular cloud (D1) with a virial mass within $R_{D1} = 2.8$ pc of $\approx 2.5 \times 10^5\,M_\odot$ (Turner et al. 2015, 2017).

Turner et al. (2000); Gorjian et al. (2001); Beck (2015) argued that the supernebula is excited by a young massive cluster still enshrouded by the parental molecular cloud D. The age of the cluster inferred by different authors falls in the range of 1Myr - 3.5Myr (see Alonso-Herrero et al. 2004; Monreal-Ibero et al. 2010; Calzetti et al. 2015; Smith et al. 2016). This system offers an excellent opportunity to study the early stages of star cluster formation. Silich & Tenorio-Tagle (2017) compared this cluster and star-forming cloud with their model and found that individual wind-driven shells cannot merge in this case. However, at that time high resolution ALMA observation of NGC 5253 were still not available. New observation with about 10 times better spatial resolution (Turner et al. 2017) revealed that cloud D, which was previously identified as a star-forming cloud is actually composed of several molecular clouds and that cloud D1 associated with the radio/infrared supernebula is much less massive and more compact than cloud D previously considered as a parental cloud for the enshrouded cluster. The molecular gas mass in D1 is very uncertain due to the high CO excitation, but is unlikely to exceed 35% of the cloud virial mass (Turner et al. 2017). Hereafter we adopt that in the central zone of cloud D1 with radius 2.8 pc gas and stars contribute 35% and 65% to the virial mass: $M_g(R_{D1}) = 8.75 \times 10^4\,M_\odot$ and $M_\star(R_{D1}) = 1.625 \times 10^5\,M_\odot$, respectively.

The comparison of the Silich & Tenorio-Tagle (2018) model predictions with new observations led to conclude that wind-driven shells stall, but parcels of hot shocked winds around individual stars should merge to form a global wind in a short time-scale (less than 10^5 years, see equations A8 and A9 in Silich & Tenorio-Tagle 2018) while ALMA observations clearly indicate that molecular gas in cloud D1 is relatively undisturbed. This led us to reexamine several physical processes not considered in the previous calculations and notice that mass loading from pre-main sequence (PMS) stars may prevent the pockets of hot shocked gas around individual massive stars from merging and thus sup-

press/delay the global star cluster wind development and the residual gas expulsion from young star-forming systems.

The paper is organized as follows. The model adopted for the residual molecular gas and stellar density distribution, the expected number of low mass PMS stars and their mass loss rates are discussed in Section 2. The gas dynamics in the shocked wind zones is discussed in Section 3. Here relevant hydrodynamic equations are formulated, different hydrodynamic regimes and the role of PMS stars are discussed. In this section we also discuss the hot gas volume filling factor, the ionized gas mass in the central zone of cloud D1 and model uncertainties and simplifications. The expected cloud D1 evolution is discussed in Section 4. Our major results and conclusions are summarized in Section 5.

2 MODEL SETUP

2.1 The star-forming molecular cloud D1

Molecular cloud D1 and the associated radio and IR supernebula parameters are derived from Gaussian fits to the CO, radio and IR integrated intensity maps and expressed in terms of FWHM (see Turner et al. 2000; Gorjian et al. 2001; Turner et al. 2015, 2017). The molecular gas distribution in a "Firecracker" molecular cloud in Antennae galaxies, a potential site to form a massive star cluster, can also be fit by a Gaussian profile (Finn et al. 2019). Therefore hereafter a Gaussian distribution for the residual gas and recently formed stars, which likely excite the radio and IR supernebula, is adopted. As the FWHMs for CO and radio/IR sources are different, we assume that the molecular gas has a shallower radial density profile than the stellar mass distribution (core radii $a = FWHM_{CO}/2.355 \approx 2.4$ pc and $b = FWHM_{Radio/IR}/2.355 \approx 0.8$ pc for the molecular gas and stars, respectively). This agrees with the comparison of Walker et al. (2016) between the distribution of stars in young stellar clusters and the distribution of gas in the proto-cluster molecular clouds. The gas, the stellar mass distribution and the number of stars per unit volume as a function of distance from the molecular cloud center then are:

$$\rho_g(r) = \frac{(1-\epsilon)M_{tot}}{(2\pi)^{3/2}a^3}\exp\left[-\frac{1}{2}\left(\frac{r}{a}\right)^2\right], \quad (1)$$

$$\rho_\star(r) = \frac{\epsilon M_{tot}}{(2\pi)^{3/2}b^3}\exp\left[-\frac{1}{2}\left(\frac{r}{b}\right)^2\right], \quad (2)$$

$$n_\star(r) = \frac{N_{star}}{(2\pi)^{3/2}b^3}\exp\left[-\frac{1}{2}\left(\frac{r}{b}\right)^2\right], \quad (3)$$

where M_{tot} is the total (stars and gas) mass of the star-forming cloud, N_{star} is the total number of stars and ϵ is the global star formation efficiency.

The gas ($M_g(r)$) and stellar ($M_\star(r)$) mass and the number of stars ($N_{star}(r)$) enclosed within a sphere of radius r are:

$$M_g(r) = (1-\epsilon)M_{tot}\left[erf\left(\frac{r}{2^{1/2}a}\right) - \left(\frac{2}{\pi}\right)^{1/2}\frac{r}{a}\exp\left[-\frac{1}{2}\left(\frac{r}{a}\right)^2\right]\right], \quad (4)$$

$$M_\star(r) = \epsilon M_{tot}\left[erf\left(\frac{r}{2^{1/2}b}\right) - \left(\frac{2}{\pi}\right)^{1/2}\frac{r}{b}\exp\left[-\frac{1}{2}\left(\frac{r}{b}\right)^2\right]\right], \quad (5)$$

$$N_{star}(r) = N_{tot}\left[erf\left(\frac{r}{2^{1/2}b}\right) - \left(\frac{2}{\pi}\right)^{1/2}\frac{r}{b}\exp\left[-\frac{1}{2}\left(\frac{r}{b}\right)^2\right]\right], \quad (6)$$

where $erf(r)$ is the error function.

The total mass of the cloud and the global star formation efficiency are determined by means of the masses $M_g(R_{D1})$ and $M_\star(R_{D1})$, radius R_{D1} and the gas and stellar density distribution core radii a and b:

$$M_{tot} = \frac{M_g(R_{D1})}{erf\left(\frac{R_{D1}}{2^{1/2}a}\right) - \left(\frac{2}{\pi}\right)^{1/2}\frac{R_{D1}}{a}\exp\left[-\frac{1}{2}\left(\frac{R_{D1}}{a}\right)^2\right]} + \frac{M_\star(R_{D1})}{erf\left(\frac{R_{D1}}{2^{1/2}b}\right) - \left(\frac{2}{\pi}\right)^{1/2}\frac{R_{D1}}{b}\exp\left[-\frac{1}{2}\left(\frac{R_{D1}}{b}\right)^2\right]} \quad (7)$$

$$\epsilon = \frac{M_\star(R_(D1)}{M_{tot}}\left[erf\left(\frac{R_{D1}}{2^{1/2}b}\right) - \left(\frac{2}{\pi}\right)^{1/2}\frac{R_{D1}}{b}\exp\left[-\frac{1}{2}\left(\frac{R_{D1}}{b}\right)^2\right]\right] \quad (8)$$

Equations (7) and (8) together with R_{D1}, $M_g(R_{D1})$ and $M_\star(R_{D1})$ obtained by Turner et al. (2017) give $M_{tot} = 4.64\times10^5$ M$_\odot$ and $\epsilon = 0.35$.

The pressure profile in such a cloud is determined by the equation of the hydrostatic equilibrium (Calura et al. 2015):

$$\frac{dP_g}{dr} = -\frac{GM(r)\rho_g(r)}{r^2}, \quad (9)$$

where G is the gravitational constant and $M(r) = M_g(r) + M_\star(r)$ is the total mass enclosed within a sphere of radius r. Numerical integration of equation (9) from a large radius where the gas pressure is negligible towards the center determines the gas pressure $P_g(r)$ at different distances from the molecular cloud center. As in molecular clouds the gas pressure is dominated by turbulence (e.g. Elmegreen & Efremov 1997; Elmegreen 2017; Johnson et al. 2015), equation (9) also allows one to obtain the gas one-dimensional velocity dispersion $\sigma^2(r) = P_g(r)/\rho_g(r)$ (Smith & Gallagher 2001). The distribution of the gas density, pressure and velocity dispersion in a Gaussian star-forming cloud with a total mass $M_{tot} = 4.64\times10^5$ M$_\odot$ global star formation efficiency $\epsilon = 0.35$ and the gas and stellar mass distribution core radii $a = 2.4$pc and $b = 0.8$pc, is shown in Fig. 1.

Following Starburst99 synthetic model we assume that

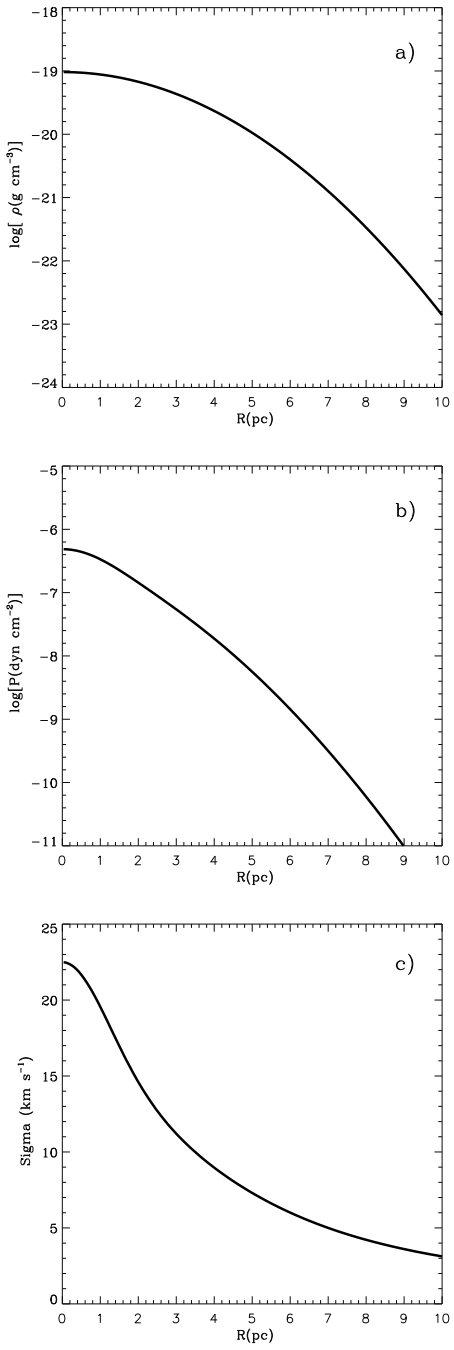

Figure 1. The star-forming cloud. Panels a, b and c display the distributions of the gas density, pressure and 1D velocity dispersion, respectively.

in a young stellar cluster with a standard Kroupa initial mass function (IMF) the number of single massive ($M > 8\,M_\odot$) stars N_{mass} scales with the star cluster mass as

$$N_{mass} \approx 10^4 (M_\star/10^6\,M_\odot). \quad (10)$$

The half distance X between neighboring massive stars at different distances from the star cluster center then is:

$$X(r) = b\left[3(\pi/2)^{1/2}\exp\left[\frac{1}{2}\left(\frac{r}{b}\right)^2\right]\right]^{1/3} N_{mass}^{-1/3}. \quad (11)$$

2.2 Massive stars mechanical luminosities and mass loss rates

Hereafter it is assumed that all massive stars are identical. The representative star mechanical power L_0, mass loss and Lyman continuum rates $\dot{M}_0$ and Q_0 are then obtained by means of Starburst99 version 7 synthetic model (Leitherer et al. 1999). Fig. 2 presents the time evolution of these quantities in the case of a standard Kroupa IMF, $Z = 0.2Z_\odot$ and the Padova stellar evolutionary tracks that include AGB stars. The representative stellar wind terminal speed falls in the range of 2600km s^{-1} - 2900km s^{-1}.

2.3 Pre-main sequence stars and their mass loss rates

The number of PMS low mass ($M \leq 3\ M_\odot$) stars can be also scaled with the star cluster mass (see Appendix A):

$$N_{PMS} \approx 1.5 \times 10^6 (M_\star/10^6\,M_\odot). \quad (12)$$

This implies that in young stellar clusters more than 100 low mass PMS stars are located in the $r \leq X$ region around each massive star. These stars have proto-stellar disks which lose mass continuously due to different processes, such as slow winds driven by the inward accretion flows (Appenzeller & Mundt 1989; Hartmann & Bae 2018) or proto-stellar disk heating by the central low mass star X-ray emission (Ercolano et al. 2008; Drake et al. 2009; Owen et al. 2011), magnetically collimated, centrifugally launched jets, Herbig-Haro objects (see Bally et al. 2007; Coffey et al. 2008; Frank et al. 2014; Nisini et al. 2018, and references therein). However, it is likely that in young, compact clusters, where distances between massive and low mass stars are small, photoevaporation of proto-stellar disks by the neighboring massive star UV radiation dominates over the other mass-loss mechanisms (Johnstone et al. 1998; Störzer & Hollenbach 1999; Richling & Yorke 2000). The proto-stellar disk mass-loss rates depend on many parameters, such as proto-stellar disk orientation, mass, distance to the massive star, UV radiation intensity and in different observations and models fall into a wide range from $10^{-9}\,M_\odot$ yr^{-1} to $10^{-6}\,M_\odot$ yr^{-1}. Analysis of pre-main sequence stellar populations in a number of stellar clusters shows that the proto-stellar disk fraction in the youngest star clusters exceeds 80%, but it decreases with the star cluster age in a relatively short time-scale of ~ 3 Myr (Haisch et al. 2001; Lada & Lada 2003; Fedele et al. 2010).

3 SUBSONIC SHOCKED WIND ZONES AROUND INDIVIDUAL MASSIVE STARS

In massive and compact young stellar clusters wind-driven shells around individual stars stall before merging with their neighbors (Silich & Tenorio-Tagle 2017) and disperse into a high pressure, turbulent intra-cloud medium. However, the hot shocked wind zones around massive stars continue to grow as their central stars supply mass and energy for a much longer time. Such hot blobs filled with shocked stellar wind gas grow in the subsonic regime until they merge with their neighbors or reach their cooling radii (Silich & Tenorio-Tagle 2018). In such shocked wind zones

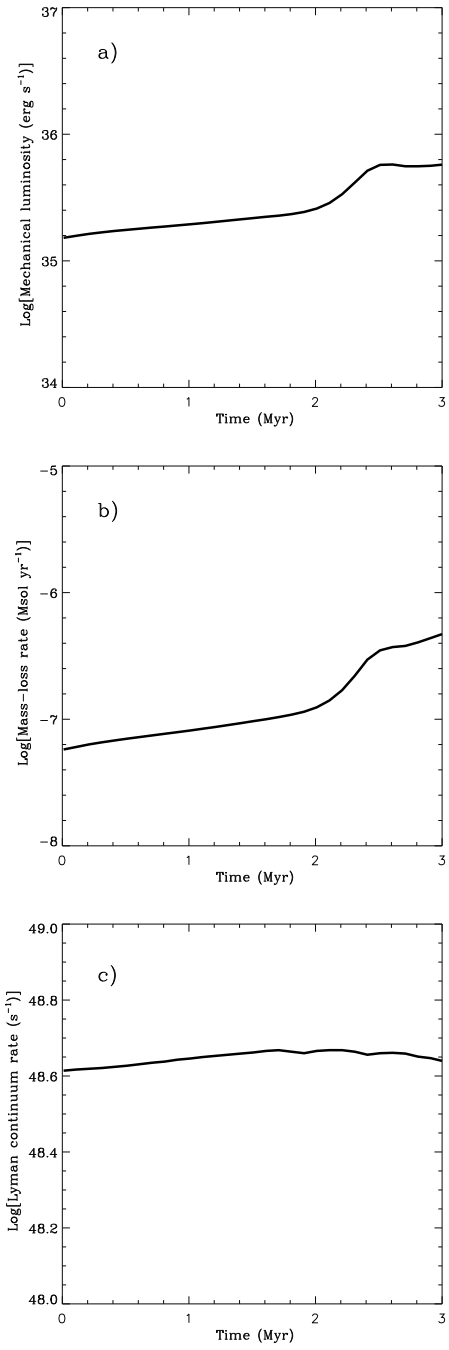

Figure 2. Massive stars input rates. The mechanical power, mass loss and Lyman continuum rates of a representative massive star.

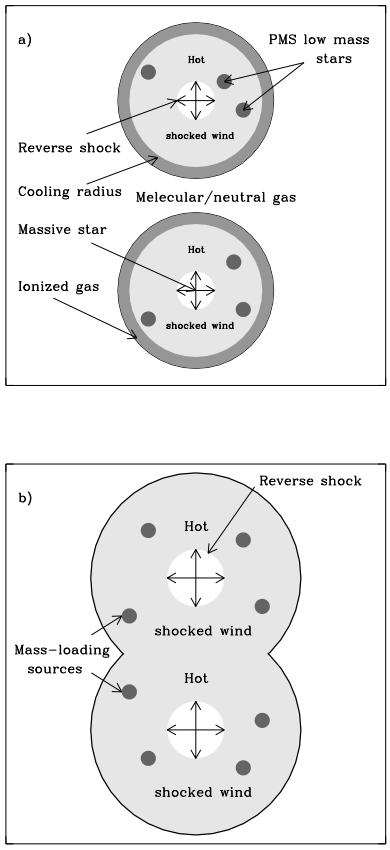

Figure 3. Schematic representation of the gas distribution around individual massive stars. Panel a shows the gas distribution in the strong radiative regime, whereas panel b shows the same in the case when radiative cooling is unable to prevent the merging of hot neighboring shocked winds.

the reverse shock radius R_{RS} is determined by the equation:

$$R_{RS} = \left(\frac{L_0}{2\pi V_\infty P_{ram}} \right)^{1/2}, \quad (13)$$

where $V_\infty = (2L_0/\dot{M}_0)^{1/2}$ is the stellar wind terminal speed (see section 2.2) and the stellar wind ram pressure P_{ram} is determined by the condition that the gas pressure at the edge of the shocked wind zone is equal to the turbulent pressure in the ambient medium. In massive and compact star-forming molecular clouds the reverse shock radii R_{RS} are small due to a large intra-cluster gas pressure. This leads to a large shocked gas density. In addition, at early stages of evolution shocked winds could be mass-loaded via photoevaporation of PMS star proto-stellar disks. This would enhance the shocked gas density and boosts cooling rates in the shocked wind zones. Thus a large intra-cluster gas pressure and mass loading may result in catastrophic shocked gas cooling at distances which are smaller than the half-distance between neighboring massive stars. In this regime shocked winds do not merge and pockets of hot gas remain immersed into cold, dense residual gas. Under such conditions, star clusters do not form a global wind and do not expel the leftover gas into the ambient ISM. Fig. 3 illustrates the two regimes. In the catastrophic cooling regime (panel a) shocked mass-loaded winds around individual massive stars cool before merging with their neighbors, whereas in the lower pressure and less mass-loaded environments the neighboring shocked winds merge (panel b in Fig. 3), fill in the cluster volume with a hot gas and expel the residual gas into the ambient ISM. In the catastrophic cooling regime the hot, the ionized and the molecular gas components live together, but as shown below, the ionized gas occupies only a small fraction of the star cluster volume whereas the size of the hot shocked wind zones around individual massive stars

and thus the hot component volume filling factor grows as the star cluster ages.

3.1 Main equations

The distribution of the gas temperature, density and pressure in the subsonic shocked wind zones around individual massive stars is determined by the steady state, spherically symmetric hydrodynamic equations which include mass loading by PMS stars as a source term. As the number of low mass PMS stars around each massive star is large, we assume that mass loading is smoothly distributed inside shocked wind zones and normalize it to the number of PMS. The mass loading rate per unit space volume q_m then is:

$$q_m = \dot{M}_{PMS}\, n_{PMS}, \tag{14}$$

where $\dot{M}_{PMS}$ is the average mass loss rate per each PMS disk and n_{PMS} is the number of PMS stars per unit volume determined by equation (3) with $N_{star} = N_{PMS}$. $\dot{M}_{PMS}$ is a free parameter of the model and is assumed to be constant. The set of the hydrodynamic equations which accounts for the mass loading and the shocked gas cooling then is (e.g. Silich et al. 2004):

$$\frac{1}{r^2}\frac{\mathrm{d}\rho u r^2}{\mathrm{d}r} = q_m, \tag{15}$$

$$\rho u \frac{\mathrm{d}u}{\mathrm{d}r} = -\frac{\mathrm{d}P}{\mathrm{d}r} - q_m u, \tag{16}$$

$$\frac{1}{r^2}\frac{\mathrm{d}}{\mathrm{d}r}\left[\rho u r^2 \left(\frac{u^2}{2} + \frac{\gamma}{\gamma-1}\frac{P}{\rho}\right)\right] = -Q, \tag{17}$$

where u, ρ and P are the gas velocity, density and thermal pressure in the shocked gas region, r is the distance from the central massive star, q_m is the mass loading rate. $Q = n_i n_e \Lambda(T, Z)$ is the cooling rate, $\Lambda(T, Z)$ is the Raymond et al. (1976) cooling function, $n_i \approx n_e$ are the ion and electron number densities in the hot shocked wind blobs and Z is the stellar wind metallicity. One can integrate equation (15) and present the set of equations (15)-(17) in a form suitable for the numerical integration:

$$\frac{\mathrm{d}u}{\mathrm{d}r} = \frac{1}{r\rho}\frac{(\gamma-1)rQ + 2\gamma u P - (\gamma+1) r q_m u^2/2}{u^2 - c^2}, \tag{18}$$

$$\frac{\mathrm{d}P}{\mathrm{d}r} = -\rho u \frac{\mathrm{d}u}{\mathrm{d}r} - q_m u, \tag{19}$$

$$\rho = \frac{\dot{M}_0}{4\pi u r^2} + \frac{q_m R_{RS}^3}{3 u r^2}\left(\frac{r^3}{R_{RS}^3} - 1\right), \tag{20}$$

where $\dot{M}_0$ is the central massive star mass loss rate, R_{RS} is the reverse shock radius and $c^2 = \gamma P/\rho$ is the sound speed in the shocked wind plasma. The temperature of the shocked wind is $T = \mu_i c^2/\gamma k$, where $\mu_i = 14/23 m_H$ is the mean mass per particle in the completely ionized gas with 1 helium atom per each 10 hydrogen atoms, m_H is the mass of the hydrogen atom and k is the Boltzmann constant. The set of equations (18) - (20) is integrated numerically outwards from the reverse shock position. The initial conditions for the numerical integration (the values of the shocked wind density, ρ_{sw}, temperature, T_{sw}, and pressure, P_{sw} behind the reverse shock) are determined by the Rankine-Hugoniot conditions at the reverse shock (see Silich & Tenorio-Tagle 2018).

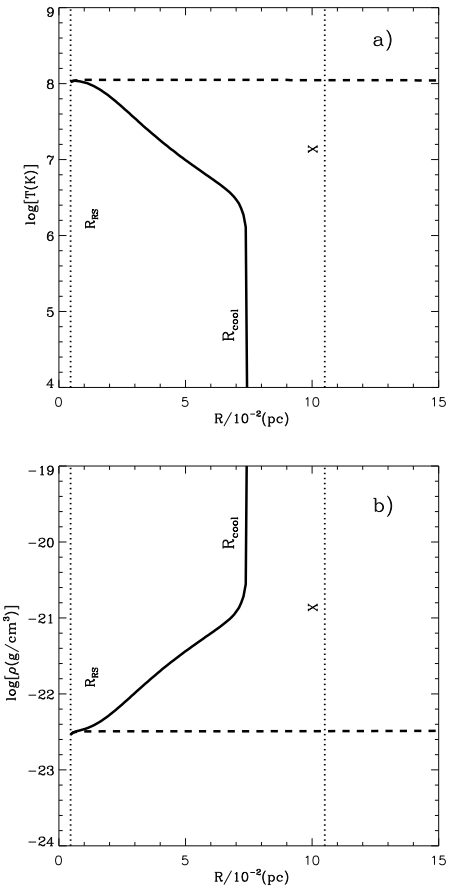

Figure 4. The temperature and density distribution around a single massive star located in the star cluster center. Panels a and b present the temperature and density distributions in the case with and without mass loading (solid and dashed lines, respectively). Dotted vertical lines show, from the left to the right, the reverse shock position and the half distance between neighboring massive stars in the star cluster center, respectively. A mass loading rate of $5 \times 10^{-8}\,\mathrm{M_\odot\ yr^{-1}}$ per each PMS star was adopted in the mass loading model.

3.2 Impact of mass loading

The distributions of the gas temperature and density within the hot blob around a representative 1 Myr old massive star located in the star cluster center are shown in Fig. 4. The cases without and with mass loading (dashed and solid lines, respectively) show very different results. Mass loading affects the temperature and density distributions around individual massive stars significantly. In the model without mass loading the shocked wind gas does not cool and neighboring hot blobs merge to form a star cluster wind, whereas in the model with mass loading the shocked gas cools before merging at $R_{cool} < X$ which prevents the expulsion of the reinserted and the residual gas from the cluster.

In order to determine if a star cluster could form a global wind or the global wind is suppressed, one should compare the cooling radii R_{cool} with the half distance X between neighboring massive stars. Fig. 5 shows how the R_{cool}/X ratio changes with distance from a 1 Myr old star cluster center if the mass loading rate per each PMS star is $\dot{M}_{PMS} =$

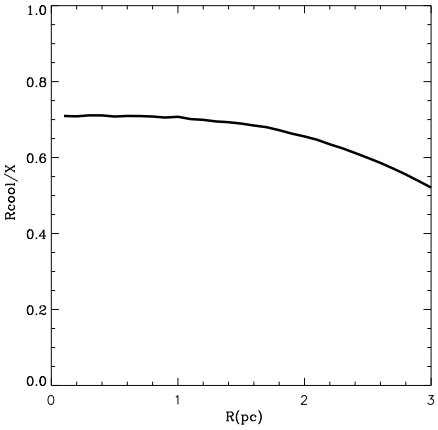

Figure 5. The R_{cool}/X ratio as a function of the distance to the star cluster center. The same assumptions regarding the mass loading rate as those used in the previous section were adopted to calculate the R_{cool} for massive stars located at different distances from the star cluster center.

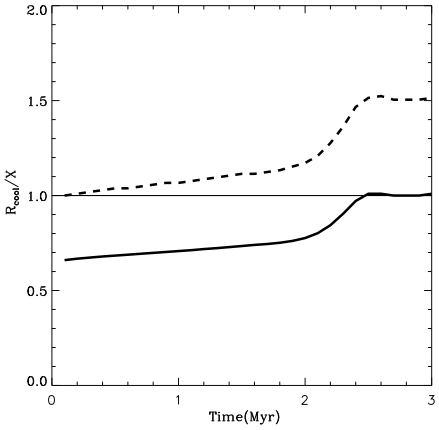

Figure 6. Cooling radius R_{cool} as a function of time. Dashed and solid lines present cooling radii normalized to a half-distance between neighboring massive stars in the star cluster center with $\dot{M}_{PMS} = 8 \times 10^{-9}\,\mathrm{M}_\odot$ yr^{-1} and $\dot{M}_{PMS} = 5 \times 10^{-8}\,\mathrm{M}_\odot$ yr^{-1} cases, respectively.

$5\times10^{-8}\,\mathrm{M}_\odot$ yr^{-1}. It is almost constant in the central zone of the cluster, where most massive stars are concentrated, and decreases at larger radii. This implies that if in the center $R_{cool} < X$, hot shocked blobs would not merge anywhere in the whole star cluster volume and the global star cluster wind would be suppressed.

The shocked gas cooling radius evolution in the star cluster center is shown in Fig. 6. Here the cooling radii are normalized to the half-distance between neighboring massive stars and compared for models with different mass loading rates. The first model (thick dashed line) assumes a conservative mass loading rate of $\dot{M}_{PMS} = 8 \times 10^{-9}\,\mathrm{M}_\odot$ yr^{-1} per each pre-main sequence star located inside the hot blob. About six times larger mass loading rate, $\dot{M}_{PMS} = 5 \times 10^{-8}\,\mathrm{M}_\odot$ yr^{-1}, was selected in the other case (thick solid line). In the case with a lower mass loading rate subsonic hot shocked winds merge and then form a global star cluster wind. However, if the average mass loading rate per PMS star exceeds $8\times10^{-9}\,\mathrm{M}_\odot$ yr^{-1}, hot shocked blobs may cool before merging. In this case the residual gas in the cluster remains for a while relatively undisturbed. The duration of this period is determined by the mass loading rate which in turn depends on the proto-stellar disks lifetime. The systematic survey for circumstellar disks in young stellar clusters indicates that the proto-stellar disk fraction decreases with the star cluster age and that about one-half of the stars within the cluster lose their disks within ~ 3 Myr (see Haisch et al. 2001; Lada & Lada 2003; Fedele et al. 2010). Therefore it is likely that in cloud D1 mass loading prevents the expulsion of the residual gas only for a few Myrs as during this time a significant number of proto-stellar disks vanishes and thus the mass loading rate in the shocked wind zones is reduced. This favors a suppressed negative stellar feedback scenario at a small cluster age and explains why the CO gas in this cluster remains relatively undisturbed.

3.3 Hot gas volume filling factor

Calculating hot blobs cooling radii $R_{cool}(r)$ at different distances from the star cluster center, one can obtain the hot gas volume filling factor f_X:

$$f_X = \frac{4\pi}{R^3}\int_0^R n_{mass}(r) R^3_{cool}(r) r^2 \mathrm{d}r, \qquad (21)$$

where $n_{mass}(r)$ is the massive star number density at different distances from the star cluster center and R is the radius of the star cluster volume over which the filling factor is calculated. As massive stars are concentrated towards the center of cloud D1, f_X depends on radius R. f_X calculated upon the assumption that $\dot{M}_{PMS} = 5\times10^{-8}\,\mathrm{M}_\odot$ yr^{-1} and $R = 1$ pc is shown in Fig. 7. There the filling factor f_X in the central zone of the cluster grows slowly from ~ 0.3 at earliest stages of evolution to ~ 0.5 at the age of 2 Myr. It enhances then rapidly due to the increasing stellar wind power (see panel a on Fig. 2) to approach unity at the age of about 2.4 Myr. Thus hot gas occupies a rather large fraction of the star cluster central zone even when a global star cluster wind is still suppressed. Grimes et al. (2005) detected a diffuse X-ray emission from the NGC 5253 star-forming region; however at the resolution of Chandra, this emission cannot be definitely associated with the D1 cluster.

3.4 The ionized gas distribution

Before shocked winds merge, Lyman continuum photons escape from the shocked wind zones and photoionize the residual gas between neighboring massive stars. Dust grains and recombining atoms absorb these photons and form ionized shells around each massive star. The ionized gas density distribution in such shells and the shell mass are determined by the set of equations (see Draine 2011;

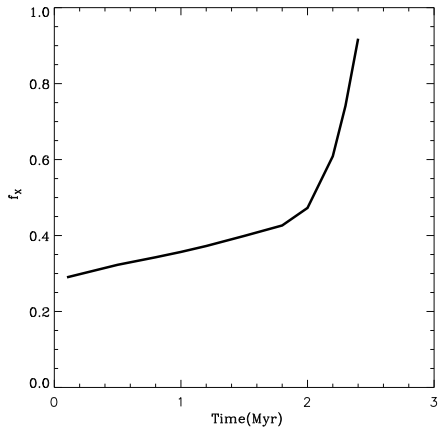

Figure 7. The hot gas filling factor f_X in the central zone of the cluster as a function of time.

Martínez-González et al. 2014):

$$\frac{d}{dr}\left(\frac{\mu_a}{\mu_i} nkT_i + \mu_a n\sigma^2\right) = n\sigma_d \frac{[L_n e^{-\tau} + L_i\phi]}{4\pi r^2 c} + n^2\beta_2 \frac{\langle h\nu\rangle_i}{c}, \quad (22)$$

$$\frac{d\phi}{dr} = -\frac{4\pi r^2 \beta_2 n^2}{Q_0} - n\sigma_d\phi, \quad (23)$$

$$\frac{d\tau}{dr} = n\sigma_d, \quad (24)$$

where $n(r)$ is the ionized gas density, Q_0 is the number of Lyman continuum photons emitted by the central star per second, L_i and L_n are the central star luminosities in ionizing and non-ionizing photons, respectively, $\phi(r)$ is the fraction of the ionizing photons that reaches a surface with radius r and $\langle h\nu\rangle_i = L_i/Q_0$ is the ionizing photons mean energy. k and c are the Boltzmann constant and the speed of light, $\beta_2 = 2.59 \times 10^{-13}$ cm^3 s^{-1} is the recombination coefficient to all but the ground level, σ_d is the effective dust absorption cross section per hydrogen atom, $\tau(r)$ is the dust optical depth and $\mu_a = 14/11 m_H$ is the mean mass per atom. $T_i = 10^4$ K is the ionized gas temperature and σ is the residual gas velocity dispersion, which depends on the massive star position inside the cluster (see panel c in Fig.2). Note that in addition to the ionized gas thermal pressure, equations (22-24) include the intra-cloud gas turbulent pressure. Following Draine (2011) we select the dust absorption cross section per hydrogen atom $\sigma_d = 10^{-21}$ cm^2 as a standard value. Equations (22-24) are integrated from the cooling radius, where $\tau = 0$ and $\phi = 1$ outwards from the central star. The initial value of n is selected from the condition that the ionized gas pressure at the inner edge of the ionized shell is equal to the gas thermal pressure inside a hot shocked wind blob. Starburst99 determines the central star mechanical power, L_i and L_n luminosities and the number of Lyman continuum photons Q_0. The location of a massive star with respect to the cluster center determines the shocked gas pressure and thus the value of the cooling radius and the ionized gas density at the inner edge $r = R_{cool}$ of

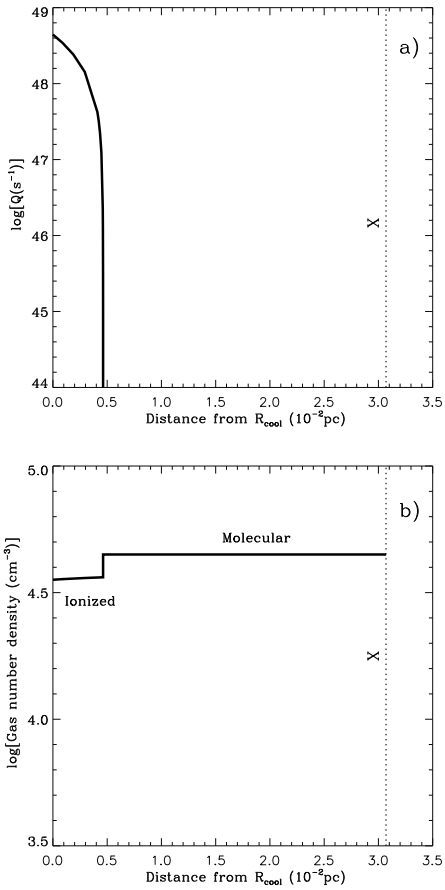

Figure 8. Ultracompact HII regions around individual massive stars. Panel a shows the ionizing photon flux and panel b the ionized gas density distribution around a representative 1 Myr old massive star accommodated in the star cluster center. The vertical dotted line displays the half-distance to a neighboring massive star.

the ionized zone. This allows one to determine the ionized zone thickness and mass around each massive star.

The Lyman continuum photon flux and the gas density distribution around a 1 Myr old massive star located in the star cluster center are shown in Fig. 8. Here a step in the gas density distribution marks the edge of the HII region and is due to the different temperatures in the turbulent ionized (10^4 K) and turbulent molecular (300 K, see Turner et al. 2015, 2017) gas components. Note that the ionized shell is thin and the ionized gas density is almost homogeneous, that implies a negligible impact of radiation pressure on the ionized shell structure.

Having masses of ionized shells around massive stars located at different distances to the star cluster center, one can obtain the total ionized gas mass M_{HII}:

$$M_{HII} = 4\pi \int_0^R n_{mass}(r) m_{HII}(r) r^2 dr, \quad (25)$$

where $n_{mass}(r)$ and $m_{HII}(r)$ are the number of massive stars per unit volume and the ionized shell mass at different distances from the star cluster center and R is the radius of the star cluster volume over which the ionized gas mass is calculated. The ionized gas mass inside a 3 pc central zone

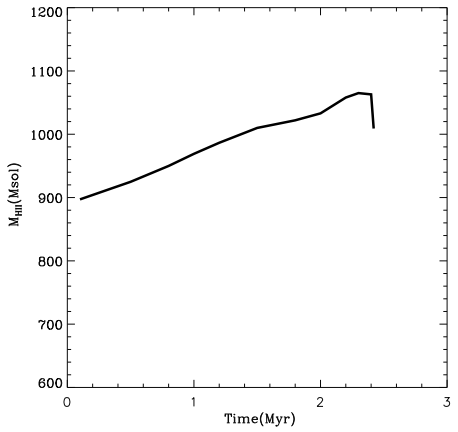

Figure 9. The ionized intra-cloud gas mass as a function of time. The ionized gas mass inside a 3 pc central zone of D1 cloud was calculated upon the assumption that the mass-loss rate per each PMS star is $5 \times 10^{-8}\,\mathrm{M}_{\odot}\ \mathrm{yr}^{-1}$.

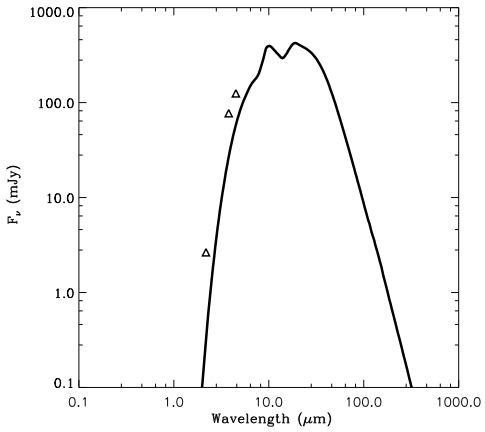

Figure 10. The model-predicted IR spectral energy distribution. Triangle symbols display the near-IR excess revealed by Vanzi & Sauvage (2004).

of the cluster at different times calculated upon the assumption that $\dot{M}_{PMS} = 5 \times 10^{-8}\,\mathrm{M}_{\odot}\ \mathrm{yr}^{-1}$ is shown in Fig. 9. The ionized gas mass in the central zone of the cluster increases slowly until hot shocked winds start to merge. The ionized gas mass drops then as no neutral/molecular gas remains in the central zone of the cluster. Lyman continuum photons then escape from the central zone to ionize gas located at larger distances from the cloud center. Note that photoionization of proto-stellar disks depends on many factors, such as the disk size, orientation, distance to the massive star and was not considered in these calculations.

D1 cluster is a very strong source of the infrared emission (Gorjian et al. 2001) whose spectral energy distribution (SED) presents a clear near-infrared excess (Alonso-Herrero et al. 2004). Here we asssume that ionized shells around massive stars are dusty and make use the theory of stochastic grain temperature fluctuations (Guhathakurta & Draine 1989; Martínez-González et al. 2016, 2017) to obtain the infrared SED associated with these dusty ultracompact HII regions located in the central zone of the cluster. The model predicted cooling radii and the ionized shell masses together with the representative 1 Myr old massive star Starburst99 spectrum and the gas-to-dust mass ratio obtained by Turner et al. (2015) (GTD=47) were used as the input parameters for these calculations. It was also assumed that dust grains have a power-low size distribution $\sim a^{-3.5}$ with the lower and upper cutoff radii $a_{min} = 0.001\mu$m and $a_{max} = 0.5\mu$m, respectively, that carbonaceous and silicate grains have an equal mass proportion.

The integrated over a star cluster volume with radius R infrared SED then is:

$$F_\nu = 4\pi \int_0^R n_{mass}(r) f_\nu(r) r^2 \mathrm{d}r, \qquad (26)$$

where $n_{mass}(r)$ and $f_\nu(r)$ are the number of massive stars per unit volume and the spectral energy distribution associated with individual massive stars located at different distances from the star cluster center, respectively. F_ν is the integrated over the star cluster volume SED. Figure 10 presents F_ν that accounts for all massive stars located within cloud D1 central zone with radius $R = 3$pc. It agrees well with the near-IR excess revealed by Vanzi & Sauvage (2004), which is displayed in Fig. 10 by the triangle symbols.

3.5 Model Uncertainties and Simplifications

In the previous sections we examined the interplay among massive star winds and the residual gas in massive star-forming molecular clouds at scales comparable to the mean separation between massive stars in the assembling cluster. Several significant simplifications were adopted to reach our major aim - to reveal physical processes which may suppress or delay a global star cluster wind development and the dispersal of the parental molecular cloud at the early, pre-supernovae, star cluster formation stage. In particular, we adopted a static distribution of stars and gas in the parental cloud and thus considered a snapshot of a more complicated dynamical process (e.g. Lahén et al. 2019, 2020). We also did not consider a possible mass segregation and thus a possible difference in massive and low mass star distributions. Another significant simplification is the assumption that all massive stars are identical whereas mechanical power and mass loss rates strongly depend upon the star mass that may lead to the formation of a more complicated structure with less massive star winds enclosed into the pockets of larger hot shocked winds formed around most massive stars. We were also unable to calculate how mass loading rate from PMS stars change with time within young massive clusters and therefore derived a lower mass loading rate per PMS star which is required to suppress the development of a global star cluster wind and delay the residual gas expulsion from the star cluster parental cloud D1. Finally, a spherical approximation used in the calculations is valid until shocked wind cooling radii remain smaller than the characteristic scale (core radius) of the residual gas distribution. This approximation is good for this particular cluster as in this case massive stars are located in the central zone of dense D1 cloud where the residual gas distribution is almost homogeneous and the calculated shocked gas cooling radii are much smaller than the molecular cloud core radius. However, it may be violated in systems with similar characteris-

tic scales for the residual gas and massive star distributions. Further understanding of early star cluster formation stages certainly would benefit from the detailed consideration of all these effects.

4 SUMMARY AND CONCLUSIONS

Here the interplay among massive stars and the residual gas in young stellar clusters was investigated. It was suggested that mass loading from PMS stars may have a significant impact on the early stages of the star cluster assembling. Mass loading slows down the flow and enhances the cooling rate in the hot shocked wind zones around massive stars that may suppress or delay a global star cluster wind development and the dispersal of the parental molecular cloud at the pre-supernovae star cluster formation stage. This effect was incorporated into the model developed in our previous papers (Silich & Tenorio-Tagle 2017, 2018) and confronted with recent observations of an obscured young stellar cluster in the center of NGC 5253 D1 molecular cloud.

Following radio, IR and CO observations, it was adopted that in the NGC 5253 D1 cluster recently formed stars are highly concentrated towards the cloud D1 center and the characteristic scales for the molecular gas and stellar mass distributions are different: ≈ 2.4 pc and ≈ 0.8 pc for the molecular gas and stars, respectively. In this case the central gas density and the central turbulent pressure are large and exceed $\sim 10^4$ cm^{-3} and 10^{-7} dyn cm^{-2}, respectively. These parameters together with the molecular cloud mass and the star formation efficiency have been used as input parameters for simulations.

The calculations without mass loading show that despite the turbulent pressure in the central zone of such molecular cloud is large, it cannot prevent neighboring hot shocked winds from merging. This is in conflict with ALMA observations which show that the CO gas in cloud D1 is relatively undisturbed. However, in the calculations with a moderate mass loading rate stellar winds do not merge at least during a few Myr. This delays the development of a global star cluster wind and the progenetor molecular cloud dispersal. The negative stellar feedback is then suppressed and the residual molecular gas remains relatively undisturbed.

These simulations show that in the case of NGC 5253 D1 cloud mass loading rates larger than $\dot{M}_{PMS} = 8 \times 10^{-9}$ M$_\odot$ yr^{-1} per each low mass PMS star are required to suppress the negative stellar feedback on the parental molecular cloud. The duration of the suppressed negative feedback stage depends on the mass loading rate, which ceases with time, and massive star mechanical luminosities, which increase with time. In the D1 cluster it may reach a few Myr. During this stage the star-forming cloud remains relatively undisturbed. Hot shocked winds cannot merge and occupy only a fraction of cloud D1 central zone. In our representative model with a constant mass loading rate of 5×10^{-8} M$_\odot$ yr^{-1} per each PMS low mass star, the hot component volume filling factor in the central 1 pc zone of the cloud is moderate ($f_X \approx 0.3$) at the earliest stages of evolution. However, it grows to unity at the age of ≈ 2.4 Myr due to increasing power of individual stellar winds.

In contrast, the ionized residual gas is concentrated in very thin, high density layers around massive stars and occupies only a small fraction of D1 cloud volume. The model predicted ionized gas mass in the central zone of the cloud (~ 1000 M$_\odot$) is smaller than estimated by Turner & Beck (2004) (~ 1900 M$_\odot$). However, the last estimate was obtained under the assumption of the ionized gas unity filling factor. A smaller filling factor would enhance the ionized gas density that, in turn, would result in a lower ionized gas mass. We thus conclude that the model predicted ionized gas mass and the immersed dust spectral energy distribution are in good agreement with the radio (Turner & Beck 2004) and near-IR Vanzi & Sauvage (2004) observations of cloud D1 and its embedded cluster.

The model explains how the impact of stellar winds on the residual molecular gas or the negative stellar feedback in NGC 5253 D1 cluster could be suppressed. However, it is unlikely that photo-evaporation of proto-stellar disks may last for a long time even at the required moderate level as the number of proto-stellar disks decreases with the star cluster age (Johnstone et al. 1998; Störzer & Hollenbach 1999; Richling & Yorke 2000). In the case of NGC 5253 D1 cloud this favors a short (a few Myrs) suppressed negative feedback scenario for the embedded cluster. It is expected that after this time hot shocked winds around individual massive stars merge and form a global star cluster wind.

APPENDIX A: PRE-MAIN SEQUENCE STARS IN YOUNG STELLAR CLUSTERS

Pre-main sequence low mass stars may contribute significantly to the mass balance in young stellar clusters. Starburst99 model does not include pre-main sequence stars contribution. Therefore here the number of low mass ($M < 3$ M$_\odot$) stars in a stellar cluster with a standard Kroupa IMF is determined. This number is used then to estimate the mass balance in hot shock-heated zones around individual massive stars. The number of stars per unit mass interval in the cluster with a broken power law IMF and lower and upper mass cutoffs M_{low} and M_{up} is:

$$N_1(m) = A m^{-\alpha_1} \qquad m \leq m_1, \tag{A1}$$

$$N_2(m) = B m^{-\alpha_2} \qquad m \geq m_1, \tag{A2}$$

where m_1 is the turnoff mass. The requirement for the IMF to be continuous at m_1 yields:

$$A = B m_1^{\alpha_1 - \alpha_2}. \tag{A3}$$

The total number of stars with masses smaller than M is:

$$N(m<M) = \frac{B}{1-\alpha_1}\left[\left(m_1^{1-\alpha_2} - \frac{M_{low}^{1-\alpha_1}}{m_1^{\alpha_2-\alpha_1}}\right) + \frac{1-\alpha_1}{1-\alpha_2}\left(M^{1-\alpha_2} - m_1^{1-\alpha_2}\right)\right]. \tag{A4}$$

The normalization coefficient B in equation (A4) is determined by the total mass of the cluster $M_\star$:

$$B = \frac{(2-\alpha_1)M_\star}{m_1^{2-\alpha_2} - \frac{M_{low}^{2-\alpha_1}}{m_1^{\alpha_2-\alpha_1}} + \frac{2-\alpha_1}{2-\alpha_2}\left(M_{up}^{2-\alpha_2} - m_1^{2-\alpha_2}\right)}. \tag{A5}$$

In the case of a standard Kroupa IMF $M_{low} = 0.1$ M$_\odot$, $M_1 = 0.5$ M$_\odot$, $\alpha_1 = 1.3$ and $\alpha_2 = 2.3$ (e.g. Leitherer et al.

1999). PMS low mass stars have masses $M < 3\,M_\odot$ (e.g. Appenzeller & Mundt 1989). Therefore the initial number of low mass PMS stars in a young stellar cluster with a Standard Kroupa IMF and an upper cutoff mass $100\,M_\odot$ scales with the star cluster mass as:

$$N_{PMS} \approx 1.5 \times 10^6 (M_\star / 10^6\,M_\odot). \quad \text{(A6)}$$

ACKNOWLEDGEMENTS

We thank the anonymous referee for many suggestions which substantially improved the original version of the paper. This study was supported by CONACYT Mxico, research grant A1-S-28458. S.M.G. also acknowledges support of CONACYT through Cátedra n.482. JT acknowledges support of NSF through grant AST1515570. The authors also acknowledge the support provided by the Laboratorio Nacional de Supercómputo del Sureste de México, CONACYT member of the national laboratories network and thank the participants of the 2019 Guillermo Haro Workshop, in particular Linda Smith, Sara Beck and Michelle Consiglio, for helpful discussions.

REFERENCES

Adams S. M., Kochanek C. S., Gerke J. R., Stanek K. Z., Dai X., 2017a, MNRAS, 468, 4968
Adams S. M., Kochanek C. S., Gerke J. R., Stanek K. Z., 2017b, MNRAS, 469, 1445
Alonso-Herrero A., Takagi T., Baker A. J., Rieke G. H., Rieke M. J., Imanishi M., Scoville N. Z., 2004, ApJ, 612, 222
Appenzeller I., Mundt R., 1989, A&ARv, 1, 291
Bally J., Reipurth B., Davis C. J., 2007, Protostars and Planets V, pp 215–230
Banerjee S., Kroupa P., 2015, MNRAS, 447, 728
Bastian N., Lardo C., 2015, MNRAS, 453, 357
Bastian N., Hollyhead K., Cabrera-Ziri I., 2014, MNRAS, 445, 378
Baumgardt H., Kroupa P., 2007, MNRAS, 380, 1589
Beck S., 2015, International Journal of Modern Physics D, 24, 1530002
Beck S. C., Turner J. L., Ho P. T. P., Lacy J. H., Kelly D. M., 1996, ApJ, 457, 610
Bedin L. R., Piotto G., Anderson J., Cassisi S., King I. R., Momany Y., Carraro G., 2004, ApJ Let, 605, L125
Boily C. M., Kroupa P., 2003, MNRAS, 338, 665
Calura F., Few C. G., Romano D., D'Ercole A., 2015, ApJ Let, 814, L14
Calzetti D., et al., 2015, ApJ, 811, 75
Carretta E., et al., 2009, A&A, 505, 117
Coffey D., Bacciotti F., Podio L., 2008, ApJ, 689, 1112
Cohen D. P., Turner J. L., Consiglio S. M., Martin E. C., Beck S. C., 2018, ApJ, 860, 47
Dale J. E., Ercolano B., Bonnell I. A., 2015, MNRAS, 451, 987
Draine B. T., 2011, ApJ, 732, 100
Drake J. J., Ercolano B., Flaccomio E., Micela G., 2009, ApJ Let, 699, L35
Elmegreen B. G., 2017, ApJ, 836, 80
Elmegreen B. G., Efremov Y. N., 1997, ApJ, 480, 235
Ercolano B., Drake J. J., Raymond J. C., Clarke C. C., 2008, ApJ, 688, 398
Fedele D., van den Ancker M. E., Henning T., Jayawardhana R., Oliveira J. M., 2010, A&A, 510, A72
Finn M. K., Johnson K. E., Brogan C. L., Wilson C. D., Indebetouw R., Harris W. E., Kamenetzky J., Bemis A., 2019, ApJ, 874, 120
Frank A., et al., 2014, Protostars and Planets VI, pp 451–474
Gorjian V., Turner J. L., Beck S. C., 2001, ApJ Let, 554, L29
Grimes J. P., Heckman T., Strickland D., Ptak A., 2005, ApJ, 628, 187
Guhathakurta P., Draine B. T., 1989, ApJ, 345, 230
Haisch Jr. K. E., Lada E. A., Lada C. J., 2001, ApJ Let, 553, L153
Hartmann L., Bae J., 2018, MNRAS, 474, 88
Johnson K. E., Leroy A. K., Indebetouw R., Brogan C. L., Whitmore B. C., Hibbard J., Sheth K., Evans A. S., 2015, ApJ, 806, 35
Johnstone D., Hollenbach D., Bally J., 1998, ApJ, 499, 758
Kim J. J., Lee Y.-W., 2018, ApJ, 869, 35
Krause M., Charbonnel C., Decressin T., Meynet G., Prantzos N., Diehl R., 2012, A&A, 546, L5
Krause M. G. H., Charbonnel C., Bastian N., Diehl R., 2016, A&A, 587, A53
Lada C. J., Lada E. A., 2003, ARA&A, 41, 57
Lahén N., Naab T., Johansson P. H., Elmegreen B., Hu C.-Y., Walch S., 2019, ApJ Let, 879, L18
Lahén N., Naab T., Johansson P. H., Elmegreen B., Hu C.-Y., Walch S., Steinwand el U. P., Moster B. P., 2020, ApJ, 891, 2
Lee Y. W., Joo J. M., Sohn Y. J., Rey S. C., Lee H. C., Walker A. R., 1999, Nature, 402, 55
Leitherer C., et al., 1999, ApJS, 123, 3
Longmore S. N., et al., 2014, Protostars and Planets VI, pp 291–314
Marino A. F., Villanova S., Piotto G., Milone A. P., Momany Y., Bedin L. R., Medling A. M., 2008, A&A, 490, 625
Martínez-González S., Silich S., Tenorio-Tagle G., 2014, ApJ, 785, 164
Martínez-González S., Tenorio-Tagle G., Silich S., 2016, ApJ, 816, 39
Martínez-González S., Wünsch R., Palouš J., 2017, ApJ, 843, 95
Mirabel F., 2017a, New Astron. Rev., 78, 1
Mirabel I. F., 2017b, in Gomboc A., ed., IAU Symposium Vol. 324, New Frontiers in Black Hole Astrophysics. pp 303–306 (arXiv:1611.09266), doi:10.1017/S1743921316012904
Monreal-Ibero A., Vílchez J. M., Walsh J. R., Muñoz-Tuñón C., 2010, A&A, 517, A27
Nisini B., Antoniucci S., Alcalá J. M., Giannini T., Manara C. F., Natta A., Fedele D., Biazzo K., 2018, A&A, 609, A87
Oey M. S., Herrera C. N., Silich S., Reiter M., James B. L., Jaskot A. E., Micheva G., 2017, ApJ Let, 849, L1
Owen J. E., Ercolano B., Clarke C. J., 2011, MNRAS, 412, 13
Portegies Zwart S. F., McMillan S. L. W., Gieles M., 2010, ARA&A, 48, 431
Rahner D., Pellegrini E. W., Glover S. C. O., Klessen R. S., 2017, MNRAS, 470, 4453
Raymond J. C., Cox D. P., Smith B. W., 1976, ApJ, 204, 290
Renzini A., et al., 2015, MNRAS, 454, 4197
Richling S., Yorke H. W., 2000, ApJ, 539, 258
Seale J. P., Looney L. W., Wong T., Ott J., Klein U., Pineda J. L., 2012, ApJ, 751, 42
Silich S., Tenorio-Tagle G., 2017, MNRAS, 465, 1375
Silich S., Tenorio-Tagle G., 2018, MNRAS, 478, 5112
Silich S., Tenorio-Tagle G., Rodríguez-González A., 2004, ApJ, 610, 226
Smith L. J., Gallagher J. S., 2001, MNRAS, 326, 1027
Smith L. J., Crowther P. A., Calzetti D., Sidoli F., 2016, ApJ, 823, 38
Störzer H., Hollenbach D., 1999, ApJ, 515, 669
Szécsi D., Wünsch R., 2019, ApJ, 871, 20
Tenorio-Tagle G., Muñoz-Tuñón C., Silich S., Cassisi S., 2015, ApJ Let, 814, L8

Tenorio-Tagle G., Silich S., Palous J., Muñoz-Tuñón C., Wunsch R., 2019, arXiv e-prints,
Thuan T. X., Sauvage M., Madden S., 1999, ApJ, 516, 783
Turner J. L., Beck S. C., 2004, ApJ Let, 602, L85
Turner J. L., Beck S. C., Ho P. T. P., 2000, ApJ Let, 532, L109
Turner J. L., Beck S. C., Benford D. J., Consiglio S. M., Ho P. T. P., Kovács A., Meier D. S., Zhao J.-H., 2015, Nature, 519, 331
Turner J. L., Consiglio S. M., Beck S. C., Goss W. M., Ho P. T. P., Meier D. S., Silich S., Zhao J.-H., 2017, ApJ, 846, 73
Vacca W. D., Johnson K. E., Conti P. S., 2002, AJ, 123, 772
Vanzi L., Sauvage M., 2004, A&A, 415, 509
Walker D. L., Longmore S. N., Bastian N., Kruijssen J. M. D., Rathborne J. M., Galván-Madrid R., Liu H. B., 2016, MNRAS, 457, 4536
Whitmore B. C., et al., 2011, ApJ, 729, 78
Wünsch R., Palouš J., Tenorio-Tagle G., Ehlerová S., 2017, ApJ, 835, 60

This paper has been typeset from a TEX/LATEX file prepared by the author.